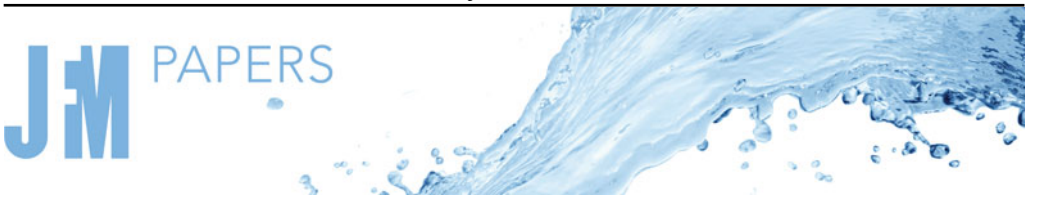
J. Fluid Mech. (2026), *vol.* 1046, A59, doi:10.1017/jfm.2026.12223



Non-equilibrium plasma formation and electromagnetic-wave scattering in hypersonic transitional flow

Zhigang Pu[1], **Junzhe Cao**[1] **and Kun Xu**[1,2]

[1]Department of Mathematics, Hong Kong University of Science and Technology, Clear Water Bay, Kowloon, Hong Kong, PR China

[2]Shenzhen Research Institute, Hong Kong University of Science and Technology, Shenzhen, PR China

Corresponding author: Kun Xu, makxu@ust.hk

(Received 1 July 2026 UTC; revised 8 September 2026 UTC; accepted 22 September 2026 UTC)

Hypersonic flows in the transitional regime exhibit strong thermochemical non-equilibrium, where conventional continuum assumptions fail. This paper presents a hybrid kinetic-fluid framework for simulating partially ionised argon plasmas under such conditions. The heavy-particle component is governed by a kinetic equation and solved using the unified gas-kinetic wave–particle (UGKWP) method, which captures flow physics from the rarefied to the continuum regime without being constrained by the mean free path scale. Electrons are modelled as a fluid with a separate temperature equation that accounts for elastic collisions and ionisation energy loss. An electromagnetic-wave solver, coupled with an auxiliary differential equation for the plasma current density, evaluates the wave scattering by the plasma. Validation against shock-tube experiments confirms the accuracy of the present algorithm. Application to a Mach 22 cylinder flow at Knudsen number 0.05 reveals three notable non-equilibrium transport effects – elevated near-wall heavy-particle density enhances ionisation near the stagnation point; non-equilibrium boundary-layer cooling lowers the electron-density peak in the shock layer; and non-equilibrium transport in the rarefied wake yields a higher downstream electron density. The thermal structure predicted by UGKWP differs significantly from that of the continuum gas-kinetic scheme (GKS), underscoring the important role of multiscale methods. These differences in ionisation further lead to distinct electromagnetic scattering patterns. Our results thus establish a link between multiscale non-equilibrium transport, plasma formation and electromagnetic blackout in hypersonic transitional flows.

Key words: hypersonic flow, rarefied gas flow

© The Author(s), 2026. Published by Cambridge University Press. This is an Open Access article, distributed under the terms of the Creative Commons Attribution licence (https://creativecommons.org/licenses/by/4.0/), which permits unrestricted re-use, distribution and reproduction, provided the original article is properly cited.

https://doi.org/10.1017/jfm.2026.12223 Published online by Cambridge University Press

1. Introduction

High-speed atmospheric entry and re-entry vehicles encounter flow regimes ranging from continuum at low altitudes to rarefied (Ivanov & Gimelshein 1998). In such conditions, ionisation inside the shock layer generates plasma that can severely attenuate or reflect electromagnetic waves, a phenomenon commonly referred to as communication blackout (Takahashi *et al.* 2014; Tian *et al.* 2014; Kundrapu *et al.* 2015; Takahashi 2016; Liu *et al.* 2023*b*). Accurate prediction of the electron number density and temperature distribution within the plasma layer is therefore critical for vehicle design and mission safety. The physical modelling of such flows, however, is challenging due to the simultaneous presence of thermal and chemical non-equilibrium in the high-altitude regime. Thermal non-equilibrium implies that the gas species are not in local thermal equilibrium, precluding a purely fluid description of the dynamics. Chemical non-equilibrium, in turn, indicates that the ionisation process is far from equilibrium under high-speed conditions. These complexities necessitate a kinetic description of the flow coupled with a finite-rate ionisation model.

To address these challenges, several numerical approaches have been developed. The direct simulation Monte Carlo (DSMC) method provides a particle-based solution to the Boltzmann equation and is accurate in the rarefied regime (Bird 1994; Boyd & Schwartzentruber 2017), but its computational cost becomes prohibitive near the continuum limit. At the opposite end, continuum solvers based on the Navier–Stokes equations are highly efficient in the continuum regime; however, they rely on small departures from Maxwellian velocity distributions and localised linear constitutive relations. Consequently, they fail to accurately capture the strong non-equilibrium velocity distributions and non-local transport effects inherent to rarefied and transitional flows. Recently, the unified gas-kinetic wave–particle (UGKWP) method has emerged as a robust alternative (Zhu *et al.* 2019; Liu *et al.* 2020; Long *et al.* 2024; Cao *et al.* 2026). The method dynamically decomposes the distribution function into a collisionless particle part and a collisional wave part, thereby bridging the entire flow regime without the time step constraints in the DSMC method. Since its inception, the UGKWP framework has been extended to plasma transport (Liu & Xu 2021; Pu *et al.* 2024*a*; Pu & Xu 2026), reaction flows (Wei *et al.* 2026), granular dynamics (Yang *et al.* 2022), radiative transfer (Liu *et al.* 2023*a*; Yang *et al.* 2025), turbulence (Yang & Xu 2026), phonon transport (Liu *et al.* 2025) and so on.

The present work extends the UGKWP framework to partially ionised argon plasmas through a hybrid kinetic-fluid model for heavy particles and electrons, coupled with a finite-rate ionisation model. This extension enables the simulation of thermochemical non-equilibrium flows from the rarefied to the continuum regime without being limited by the mean free path scale. The heavy-particle component is governed by a kinetic equation that includes elastic collisions and inelastic ionisation operators. The electron temperature is advanced via a macroscopic energy equation that accounts for elastic energy exchange with heavy particles and ionisation energy loss. The ionisation kinetics include two ionisation channels, namely thermal ionisation and electron-impact ionisation, proposed by Hoffert and Lien (Hoffert & Lien 1967), with forward and backward rates derived from a linear collision cross-section assumption. The overall algorithm is validated against a benchmark shock-tube experiment (Petschek & Byron 1957). The model is subsequently applied to a Mach 22 cylinder flow at a Knudsen number of 0.05. The computed plasma fields are then used as input for an electromagnetic-wave simulation. A comparative analysis between the UGKWP and gas-kinetic scheme (GKS) results is performed for both the flow and electromagnetic field solutions – a comparison rarely conducted in hypersonic flow studies due to the lack of suitable computational tools.

https://doi.org/10.1017/jfm.2026.12223 Published online by Cambridge University Press

The paper is organised as follows. Section 2 details the hybrid kinetic-fluid model employed in this study. Section 3 describes the numerical methods. Section 4 shows the shock-tube validation results. Section 5 presents the non-equilibrium plasma formation around a hypersonic cylinder and § 6 shows the electromagnetic scattering analyses. Finally, § 7 summarises the main conclusions.

2. Physical model

2.1. *Kinetic model for partially ionised argon gas*

2.1.1. *General framework*

We formulate the kinetic evolution of a partially ionised argon plasma using the coupled Boltzmann equations for neutral atoms (n), ions (i) and electrons (e)

$$\frac{\partial f_n}{\partial t} + \boldsymbol{u}\cdot\nabla_{\boldsymbol{x}} f_n = Q_n^{el} + Q_n^{ion}, \tag{2.1}$$

$$\frac{\partial f_i}{\partial t} + \boldsymbol{u}\cdot\nabla_{\boldsymbol{x}} f_i + \frac{e\boldsymbol{E}}{m_i}\cdot\nabla_{\boldsymbol{u}} f_i = Q_i^{el} + Q_i^{ion}, \tag{2.2}$$

$$\frac{\partial f_e}{\partial t} + \boldsymbol{u}\cdot\nabla_{\boldsymbol{x}} f_e - \frac{e\boldsymbol{E}}{m_e}\cdot\nabla_{\boldsymbol{u}} f_e = Q_e^{el} + Q_e^{ion}. \tag{2.3}$$

Here, $f_s(\boldsymbol{x}, \boldsymbol{u}, t)$ denotes the velocity distribution function of species s ($s = n, i, e$); $\boldsymbol{x}$ and $\boldsymbol{u}$ are the position and microscopic velocity vectors, t is time, e is the elementary charge and $\boldsymbol{E}$ is the electric field. The right-hand side operators separate into elastic collisions (Q_s^{el}) and the inelastic collisions of ionisation and recombination (Q_s^{ion}).

When atoms and ions remain tightly coupled through frequent collisions, they share a common velocity and temperature distribution and can be merged into a single heavy-particle component. Defining the heavy-particle distribution function $f_h \equiv f_n + f_i$, the degree of ionisation $\alpha \equiv n_i/(n_n + n_i)$ and the mean heavy-particle mass $m_h \equiv m_n \approx m_i$ (where m_n and m_i denote the neutral atom and ion masses, respectively), the kinetic equation for the heavy species reduces to

$$\frac{\partial f_h}{\partial t} + \boldsymbol{u}\cdot\nabla_{\boldsymbol{x}} f_h + \alpha\frac{e\boldsymbol{E}}{m_h}\cdot\nabla_{\boldsymbol{u}} f_h = Q_{hh}^{el}(f_h) + Q_{he}^{el}(f_h, f_e) + Q_n^{ion} + Q_i^{ion}. \tag{2.4}$$

Appendix A shows a detailed derivation of the above equation, where $Q_{hh}^{el}(f_h)$, $Q_{he}^{el}(f_h, f_e)$ on the right-hand side describe elastic collisions among heavy particles and between heavy particles and electrons, respectively. Their detailed formulations are elaborated in the subsequent parts. The electrostatic force term acts only on ions, i.e. the fraction α of the heavy component and is therefore scaled by the local ionisation degree. Ambipolar diffusion is neglected in the present study, as ambipolar effects exert a negligible influence in the simulated flow conditions.

Regarding the description of electrons, we assume that electron–electron collisions are sufficiently frequent to maintain the electrons in local thermodynamic equilibrium, thereby justifying a fluid description. Under the quasi-neutrality condition $n_i \approx n_e$, the electron continuity equation becomes redundant, as the electron number density is directly obtained from the ion density. The ion density itself is governed by the zeroth-order velocity moment of the ion kinetic equation, (2.2), which yields

$$\frac{\partial \rho_i}{\partial t} + \nabla\cdot(\rho_i \boldsymbol{U}) = m_h \dot{n}_e, \tag{2.5}$$

https://doi.org/10.1017/jfm.2026.12223 Published online by Cambridge University Press

where $\rho_i = m_h n_i$ is the ion mass density and $\dot{n}_e$ denotes the volumetric production rate of electrons (and, by charge neutrality, of ions). The expression for $\dot{n}_e$ will be introduced in a subsequent section. Following the definition of the ionisation degree $\alpha = n_i/n$, with $n = n_n + n_i$ the total heavy-particle number density, and writing the total heavy-particle mass density as $\rho = m_h n$, the ion conservation equation transforms into

$$\frac{\partial(\rho\alpha)}{\partial t} + \nabla \cdot (\rho\alpha \boldsymbol{U}) = m_h \dot{n}_e. \tag{2.6}$$

Once α is known from this equation, the number densities of all species follow directly

$$n_n = (1-\alpha)n,\ n_i = \alpha n,\ n_e = \alpha n. \tag{2.7}$$

The macroscopic velocity of the electrons is assumed to be close to that of the heavy particles ($\boldsymbol{U}_e \approx \boldsymbol{U}_h$), allowing the momentum slip and associated frictional drag between the two species to be neglected. Consequently, in the asymptotic limit of negligible electron mass ($m_e \to 0$), the electron momentum equation reduces to a force balance between the electron pressure gradient and the self-consistent electrostatic field

$$\nabla p_e = -n_e e \boldsymbol{E}. \tag{2.8}$$

Accordingly, the governing equation for the electron thermal energy is formulated as

$$\rho_e c_{v,e} \left(\frac{\partial T_e}{\partial t} + \boldsymbol{U}_e \cdot \nabla T_e \right) = \nabla \cdot (\kappa_e \nabla T_e) - p_e (\nabla \cdot \boldsymbol{U}_e) + S_{eh} + S_e^{ion}, \tag{2.9}$$

where the left-hand side represents the material derivative of the electron internal energy and $c_{v,e} = (3/2)R_e$ is the constant-volume heat capacity of electrons. The right-hand side terms account for thermal conduction (κ_e denotes the electron thermal conductivity), compressive work, the energy exchange rate with the heavy-particle species (S_{eh}) and the energy source term due to ionisation–recombination reactions (S_e^{ion}), respectively.

By substituting the electron momentum balance equation (2.8) into the heavy-particle kinetic equation (2.4) and combining it with the degree of ionisation equation (2.6) and the electron energy transport model equation (2.9), the coupled kinetic-fluid governing system is established as follows:

$$\frac{\partial f_h}{\partial t} + \boldsymbol{u} \cdot \nabla_{\boldsymbol{x}} f_h - \frac{\nabla p_e}{\rho_h} \cdot \nabla_{\boldsymbol{u}} f_h = Q_{hh}^{el}(f_h) + Q_{he}^{el}(f_h, f_e) + Q_n^{ion} + Q_i^{ion}, \tag{2.10}$$

$$\rho_e c_{v,e} \left(\frac{\partial T_e}{\partial t} + \boldsymbol{U}_e \cdot \nabla T_e \right) = \nabla \cdot (\kappa_e \nabla T_e) - p_e (\nabla \cdot \boldsymbol{U}_e) + S_{eh} + S_e^{ion}, \tag{2.11}$$

$$\frac{\partial(\rho\alpha)}{\partial t} + \nabla \cdot (\rho\alpha \boldsymbol{U}) = m_h \dot{n}_e. \tag{2.12}$$

Further simplifications can be introduced to the above system. First, in the weakly ionised regime where $n_e \ll n_h$, the electron pressure is negligible compared with the heavy-particle pressure ($p_e \ll p_h$). Consequently, the electron pressure gradient term in (2.10) may be omitted. Second, following the widely adopted approximation for the electron energy equation (Petschek & Byron 1957; Morgan & Morrison 1965; Hoffert & Lien 1967), we retain only the dominant contributions from elastic energy exchange between electrons and heavy particles and from ionisation energy loss. The reduced governing system is expressed as

https://doi.org/10.1017/jfm.2026.12223 Published online by Cambridge University Press

$$\frac{\partial f_h}{\partial t} + \boldsymbol{u} \cdot \nabla_{\boldsymbol{x}} f_h = Q_{hh}^{el}(f_h) + Q_{he}^{el}(f_h, f_e) + Q_n^{ion} + Q_i^{ion}, \tag{2.13}$$

$$\rho_e c_{v,e} \frac{\partial T_e}{\partial t} = S_{eh} + S_e^{ion}, \tag{2.14}$$

$$\frac{\partial(\rho\alpha)}{\partial t} + \nabla \cdot (\rho\alpha \boldsymbol{U}) = m_h \dot{n}_e. \tag{2.15}$$

2.1.2. *Elastic collision operators*

Next, the explicit formulations of the collision operators are detailed. The heavy-particle elastic collision operator, Q_{hh}^{el}, is modelled using the Bhatnagar–Gross–Krook (BGK) relaxation approximation

$$Q_{hh}^{el} = \frac{g_h - f_h}{\tau_h}, \tag{2.16}$$

where g_h denotes the local Maxwellian equilibrium distribution function, defined as

$$g_h = \rho_h \left(\frac{m_h}{2\pi k_B T_h}\right)^{3/2} \exp\left[-\frac{m_h}{2k_B T_h}(\boldsymbol{u} - \boldsymbol{U}_h)^2\right]. \tag{2.17}$$

Here, ρ_h, $\boldsymbol{U}_h$ and T_h represent the total mass density, macroscopic bulk velocity and temperature of the heavy-particle mixture, respectively, and k_B is the Boltzmann constant. The characteristic relaxation time τ_h is calculated as $\tau_h = 1/(1/\tau_{hh} + 1/\tau_{he})$, where τ_{hh} is the mean collision time between heavy particles and τ_{he} is the mean collision time between heavy particles and electrons. In the weakly ionised regime ($\alpha \ll 1$), the collision model of the atom–ion mixture is approximated by that of pure neutral atoms. Specifically, $\tau_{hh} = 1/(\chi_{hh} n_h)$, and the interaction coefficient χ_{hh} is

$$\chi_{hh} = \frac{(5 - 2\omega)(7 - 2\omega)\sqrt{\pi}}{15} \left(\frac{4k_B T_h}{m_h}\right)^{1/2} d_h^2, \tag{2.18}$$

where d_h represents the diameters of the heavy particles. The temperature modifies the molecular diameter as $(d/d_{ref})^2 = (T/T_{ref})^{(1/2)-\omega}$, where ω is the power coefficient between viscosity and temperature (Bird 1994); $\omega = 0.81$ is used for argon atoms, $\tau_{he} = \tau_{eh}/\alpha = 1/(\nu_{eh}\alpha)$ and ν_{eh} is detailed in the subsequent part in this section.

The collision term Q_{he}^{el} denotes cross-species collision between electrons and heavy particles and is denoted as

$$Q_{he}^{el} = \frac{g^M - g_h}{\tau_h}, \tag{2.19}$$

where g^M denotes the local Maxwell distribution after the collision with electrons, which reads

$$g^M = \rho_h \left(\frac{m_h}{2\pi k_B \bar{T}_h}\right)^{3/2} \exp\left[-\frac{m_h}{2k_B \bar{T}_h}(\boldsymbol{u} - \bar{\boldsymbol{U}}_h)^2\right]. \tag{2.20}$$

The post-collision temperature $\bar{T}_h$ is given as

$$\bar{T}_h = T_h + \tau_h \frac{4m_{he}\sigma_{s,he} v_{th,e} n_e}{m_h + m_e} (T_e - T_h), \tag{2.21}$$

https://doi.org/10.1017/jfm.2026.12223 Published online by Cambridge University Press

where the reduced mass is $m_{he} = (m_h m_e)/(m_h + m_e)$, and $\sigma_{s,he}$ denotes the collision cross-section of heavy particles and electrons, $v_{th,e}$ is the mean thermal speed of electrons. Under the assumption that electrons and heavy particles move with the same velocity, the cross-species post-collision velocity remains invariant, yielding $\bar{\boldsymbol{U}}_h = \boldsymbol{U}_h$.

The energy exchange term S_{eh}^{el} in (2.9) accounts for elastic collisional transfer of thermal energy between electrons and heavy particles. The exchange rate can be derived from the elastic collision integral and is given by

$$S_{eh}^{el} = 6n_e \frac{m_e}{m_h} \nu_{eh} k_B (T_h - T_e), \tag{2.22}$$

where ν_{eh} and ν_{ei} are the electron and heavy-particle collision frequencies. The collision frequency is computed as

$$\nu_{eh} = \nu_{en} + \nu_{ei} = n_n \sigma_{s,en} v_{th,e} + n_i \sigma_{s,ei} v_{th,e}, \tag{2.23}$$

with $\sigma_{s,en}$ and $\sigma_{s,ei}$ the electron–atom and electron–ion momentum-transfer scattering cross-section, respectively, and $v_{th,e} = \sqrt{8k_B T_e/(\pi m_e)}$. For the electron–atom cross-section, we use the piecewise fit by Jaffrin (1965)

$$\sigma_{s,en} = \begin{cases} \left(-0.35 + 0.775 \times 10^{-4} T_e\right) \times 10^{-20}\ \mathrm{m}^2 & T_e \geq 10^4\ \mathrm{K}, \\ \left(0.39 - 0.551 \times 10^{-4} T_e + 0.595 \times 10^{-8} T_e^2\right) \times 10^{-20}\ \mathrm{m}^2 & T_e < 10^4\ \mathrm{K}. \end{cases} \tag{2.24}$$

For the electron–ion cross-section (Sutton & Sherman 2006)

$$\sigma_{s,ei} = \frac{2\pi e^4}{9k_B^2 T_e^2} \ln\left(\frac{9k_B^3 T_e^3}{4\pi e^6 n_e}\right) = 1.95 \times 10^{-10} T_e^{-2.0} \ln\left(1.53 \times 10^8 \frac{T_e^3}{n_e}\right)\ \mathrm{m}^2 \quad . \tag{2.25}$$

The thermal conductivity of electrons $\kappa_e = (5/2) R_e p_e \tau_e$, where $R_e = k_B/m_e$ is the specific gas constant for electrons and τ_e is the electron mean relaxation time given as

$$\tau_e = \frac{1}{\nu_{ee} + \nu_{eh}}, \tag{2.26}$$

where the electron–electron collision frequency is given by (Braginskii 1965; Angus *et al.* 2025)

$$\nu_{ee} = \frac{n_e \ln \Lambda_{ee}}{2.7518 \times 10^5 T_e^{3/2}}, \tag{2.27}$$

where $\ln \Lambda_{ee} = 10$ is the Coulomb logarithm.

2.1.3. *Inelastic collision operators*

We now introduce the treatment of inelastic collision operators. The ionisation model adopted in this study comprises thermal ionisation (TI) and electron-impact ionisation (EI) (Hoffert & Lien 1967)

$$\begin{aligned} TI: &\quad Ar + Ar \rightleftharpoons Ar^+ + e^- + Ar, \\ EI: &\quad Ar + e^- \rightleftharpoons Ar^+ + e^- + e^-. \end{aligned} \tag{2.28}$$

https://doi.org/10.1017/jfm.2026.12223 Published online by Cambridge University Press

The forward rate coefficients are

$$k_{fA}(T_h) = 1.68 \times 10^{-26}\, T_h^{1.5} \left(\frac{\Theta^*_{A,1}}{T_h} + 2\right) \exp\left(-\frac{\Theta^*_{A,1}}{T_h}\right),$$
$$k_{fe}(T_e) = 3.75 \times 10^{-22}\, T_e^{1.5} \left(\frac{\Theta^*_{A,1}}{T_e} + 2\right) \exp\left(-\frac{\Theta^*_{A,1}}{T_e}\right), \tag{2.29}$$

and the backward (recombination) rate coefficients are

$$k_{rA}(T_h) = 5.80 \times 10^{-49} \left(\frac{\Theta^*_{A,1}}{T_h} + 2\right) \exp\left(\frac{\Theta_{ion} - \Theta^*_{A,1}}{T_h}\right),$$
$$k_{re}(T_e) = 1.29 \times 10^{-44} \left(\frac{\Theta^*_{A,1}}{T_e} + 2\right) \exp\left(\frac{\Theta_{ion} - \Theta^*_{A,1}}{T_e}\right). \tag{2.30}$$

Here, $\Theta^*_{A,1} = \epsilon^*_{A,1}/k_B = 135\,300$ K is the characteristic temperature of the first excited state of argon, with $\epsilon^*_{A,1}$ the characteristic energy, and $\Theta_{ion} = \epsilon_{ion}/k_B = 183\,100$ K is the characteristic temperature for first ionisation, with ϵ_{ion} the characteristic energy also. Unlike the conventional Arrhenius form, these expressions follow from the assumption that the inelastic cross-section varies linearly with the collisional kinetic energy (Hoffert & Lien 1967), which produces the additional factor $\Theta^*_{A,1}/T + 2$. The forward and reverse reaction rates satisfy the principle of detailed balance, naturally recovering the expected Saha equilibrium limit.

Rather than evaluating the full Boltzmann collision integrals for ionisation and recombination, we treat these inelastic processes through their velocity moments, which supply the necessary source terms for the macroscopic fluid equations. For the heavy species, the zeroth-order moment of the inelastic operators vanishes because the total number of heavy particles is conserved during ionisation and recombination

$$\int m_h \left(Q_n^{ion} + Q_i^{ion}\right) \mathrm{d}\boldsymbol{u} = 0. \tag{2.31}$$

The second-order moment gives the net energy exchange rate of the heavy particles with the ionisation process

$$\int \frac{1}{2} m_h |\boldsymbol{u}|^2 \left(Q_n^{ion} + Q_i^{ion}\right) \mathrm{d}\boldsymbol{u} = S_h^{ion}, \tag{2.32}$$

where S_h^{ion} represents the energy source term associated with TI. It is modelled as

$$S_h^{ion} = -\epsilon_{ion}\, [\dot{n}_e]_{TI}, \tag{2.33}$$

with $[\dot{n}_e]_{TI}$ denoting the net electron production rate by atom–atom collisions. For electrons, the corresponding energy loss due to EI is

$$S_e^{ion} = -\epsilon_{ion}\, [\dot{n}_e]_{EI}, \tag{2.34}$$

where $[\dot{n}_e]_{EI}$ is the net electron production rate by electron-impact collisions. The ionisation energy source terms S_h^{ion} and S_e^{ion} enter the heavy-particle and electron energy equations, respectively. The coupling between these macroscopic source terms and the microscopic distribution function is detailed in the numerical methods section.

https://doi.org/10.1017/jfm.2026.12223 Published online by Cambridge University Press

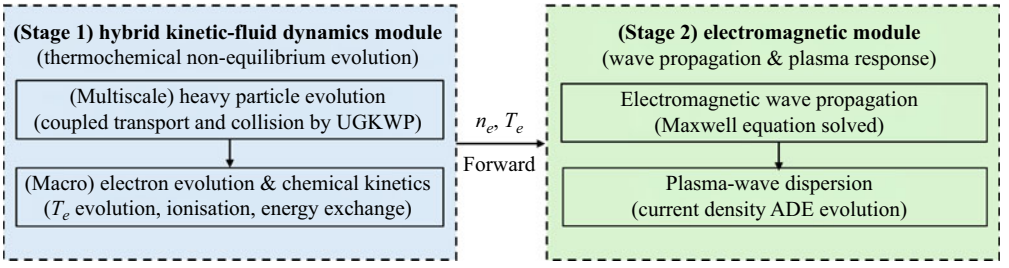


Figure 1. Flowchart of the hybrid kinetic-fluid and electromagnetic simulation framework. Stage 1 resolves the thermochemical non-equilibrium gas dynamics: the heavy-particle transport is handled by the multiscale UGKWP method from the rarefied to the continuum regime, and the electron temperature is advanced macroscopically. The electron number density n_e and temperature T_e are then passed to stage 2, where electromagnetic-wave propagation and the plasma response are simulated using a Maxwell solver and the current density ADE formulation, respectively.

The net electron production rate from each channel is expressed in terms of the number densities as

$$[\dot{n}_e]_{TI} = k_{fA} n_n^2 - k_{rA} n_i n_e n_n,$$
$$[\dot{n}_e]_{EI} = k_{fe} n_n n_e - k_{re} n_i n_e^2. \tag{2.35}$$

The total electron production rate $\dot{n}_e = [\dot{n}_e]_{TI} + [\dot{n}_e]_{EI}$ is given by substituting relation (2.7) into the above formula

$$\dot{n}_e = n^2(1-\alpha)\big[k_{fA}(1-\alpha) + k_{fe}\alpha\big] - n^3\alpha^2\big[k_{rA}(1-\alpha) + k_{re}\alpha\big]. \tag{2.36}$$

This expression directly provides the source term $S = m_h \dot{n}_e$ required in the ionisation-degree equation (2.6).

2.2. *Auxiliary differential equation for plasma medium*

We model the plasma's response to the electromagnetic field using an auxiliary differential equation (ADE) (Sun *et al.* 2018). The current density equation capturing plasma oscillation and collisional effects is

$$\frac{\partial \boldsymbol{J}}{\partial t} + \nu_{eh} \boldsymbol{J} = \epsilon_0 \omega_p^2 \boldsymbol{E}, \tag{2.37}$$

where $\boldsymbol{J}$ is the current density and ν_{eh} the electron collision frequency with heavy particles, as introduced in the previous section. The plasma frequency $\omega_p = \sqrt{n_e e^2/m_e \epsilon_0}$, and ϵ_0 is the vacuum permittivity.

3. Numerical method

3.1. *General procedure*

The overall simulation comprises two modules. The first module solves the hybrid kinetic-fluid reactive gas dynamics and supplies the electron number density n_e and temperature T_e to the second module. The second module computes the electromagnetic-wave propagation and plasma dispersion. The complete workflow is depicted in figure 1.

The time integration of the thermochemical non-equilibrium flow in the first module employs an operator-splitting procedure. Within each time step $\Delta t = t^{n+1} - t^n$, the following substeps are executed sequentially.

https://doi.org/10.1017/jfm.2026.12223 Published online by Cambridge University Press

Step 1: heavy-particle transport. The heavy-particle transport is handled by the multiscale UGKWP method from the rarefied to the continuum regime

$$\boldsymbol{W}_h^* = \mathcal{L}_1^{fl}\left(\boldsymbol{W}_h^n\right), \tag{3.1}$$

where $\mathcal{L}_1^{fl}$ denotes the UGKWP algorithm.

Step 2: chemical reactions and two-temperature coupling. The ionisation kinetics and the accompanying energy exchange are integrated locally

$$\left(\alpha^{n+1}, T_h^{**}, T_e^{**}\right) = \mathcal{L}_2^{fl}\left(\alpha^*, T_h^*, T_e^*\right). \tag{3.2}$$

The updated temperatures and ionisation fraction are then mapped back to the conservative variables through

$$\boldsymbol{W}^{**} = \mathcal{H}(\boldsymbol{W}^*), \tag{3.3}$$

where $\mathcal{H}$ enforces consistency between primitive and conservative states.

Step 3: elastic energy relaxation. The electron–heavy-particle thermal relaxation is applied

$$\left(T_h^{n+1}, T_e^{n+1}\right) = \mathcal{L}_3^{fl}\left(T_h^{**}, T_e^{**}\right). \tag{3.4}$$

A final conservative projection, $\boldsymbol{W}^{n+1} = \mathcal{H}(\boldsymbol{W}^{**})$, completes the time advancement of the gas-dynamics module.

The electromagnetic module advances in two steps.

Step 1: electromagnetic-wave propagation. The source-free Maxwell equations are solved using a GKS scheme (Pu *et al.* 2024*b*) to propagate the electromagnetic fields

$$\boldsymbol{Q}^* = \mathcal{L}_1^{em}(\boldsymbol{Q}^n), \tag{3.5}$$

where $\boldsymbol{Q} = (\boldsymbol{E}, \boldsymbol{B})$ denotes the macroscopic electromagnetic variables.

Step 2: plasma wave dispersion. The ADE for the current density is coupled implicitly with Ampere's law to evolve the current density and the electric field concurrently

$$\boldsymbol{Q}^{n+1} = \mathcal{L}_2^{em}(\boldsymbol{Q}^*). \tag{3.6}$$

3.2. *The UGKWP method for coupled transport and collision step*

First, we introduce algorithms for solving $\mathcal{L}_1^{fl}$, where $\mathcal{L}_1^{fl}$ describes kinetic transport and collision. We solve it using the UGKWP method, which removes the time step restriction imposed by the mean collision time in the near-continuum regime. The core idea of the UGKWP method is to couple the evolution of collision and free transport rather than treating them in a split manner as in purely particle methods such as the DSMC method (Zhu *et al.* 2019; Liu *et al.* 2020). In the framework of the finite volume method (FVM), the time-dependent solution of the distribution function at a cell interface can be written as

$$f\left(\boldsymbol{x}, \boldsymbol{u}, t\right) = \frac{1}{\tau}\int_0^t g(\boldsymbol{x}', \boldsymbol{u}, t')e^{-(t-t')/\tau}\mathrm{d}t' + e^{-t/\tau} f_0\left(\boldsymbol{x} - \boldsymbol{u}t\right), \tag{3.7}$$

where τ is the local mean relaxation time, f_0 is the initial gas distribution function at $t = 0$ and g is the equilibrium distribution along the characteristic line $\boldsymbol{x}' = \boldsymbol{x} - \boldsymbol{u}t'$. The equation implies that a particle has a probability of $e^{-t/\tau}$ to freely stream during the time interval $[0, t]$, and a probability of $(1 - e^{-t/\tau})$ to collide with other particles.

Based on this physical picture, the UGKWP method represents the velocity distribution function in a wave–particle coupled manner. For particles that experience collisions

https://doi.org/10.1017/jfm.2026.12223 Published online by Cambridge University Press

(the fraction $1-e^{-t/\tau}$), we assume they enter a near-equilibrium distribution. Their contribution to the numerical flux is captured analytically through the equilibrium distribution g, which is determined from the macroscopic variables. The remaining collisionless particles are represented by stochastic simulation particles $P_k(m_k, \boldsymbol{x}_k, \boldsymbol{u}_k)$. Here, m_k is the mass of a simulation particle P_k, corresponding to a cluster of real gas particles; $\boldsymbol{x}_k$ and $\boldsymbol{u}_k$ are its position and velocity, respectively. This approach removes the constraints that require the time step and mesh size to be smaller than the mean collision time and the mean free path.

In the procedure above, we require the exact macroscopic variables to determine the local equilibrium distribution. In the FVM framework, the cell-averaged macroscopic conservative variables on a physical cell Ω_i are updated by the numerical flux through cell interfaces

$$(\boldsymbol{W})_i^* = (\boldsymbol{W})_i^n - \frac{\Delta t}{|\Omega_i|}\sum_{s\in\partial\Omega_i}|l_s|(F_{\boldsymbol{W}})_s, \tag{3.8}$$

where $l_s \in \partial\Omega_i$ is the cell interface with centre $\boldsymbol{x}_s$ and outer unit normal vector $\boldsymbol{n}_s$ and $|l_s|$ is the area of the cell interface. The numerical flux across the interface $(F_{\boldsymbol{W}})_s$ can be evaluated from distribution function at the interface

$$(F_{\boldsymbol{W}})_s = \frac{1}{\Delta t}\int_{t^n}^{t^{n+1}} \boldsymbol{u}\cdot\boldsymbol{n}_s f(\boldsymbol{x}_s, \boldsymbol{u}, t)\boldsymbol{\Psi}\mathrm{d}\boldsymbol{u}\mathrm{d}t, \tag{3.9}$$

where $\boldsymbol{\Psi} = (1, \boldsymbol{u}, (1/2)|\boldsymbol{u}|^2)$ is the conservative moments of distribution functions. For the cell interface l_s, the distribution function $f(\boldsymbol{x}_s, \boldsymbol{u}, t)$ requires direct tracking of its evolution in a wave–particle manner as introduced previously. This numerical flux of the macroscopic conservative variable can be split into the equilibrium flux and free-streaming flux according to (3.7). The equilibrium flux is

$$(F_{\boldsymbol{W}})_s^g = \frac{1}{\Delta t}\int \boldsymbol{u}\cdot\boldsymbol{n}_s\left(C_1 g_0 + C_2\boldsymbol{u}\cdot\boldsymbol{g}_{0x} + C_3 g_{0t}\right)\boldsymbol{\Psi}\mathrm{d}\boldsymbol{u}, \tag{3.10}$$

where g_0 is the equilibrium distribution function on the cell interface, g_{0x}, g_{0t} are the spatial and temporal slopes of g_0. Detailed derivations of these terms can be found in Pu & Xu (2025). The time integration coefficients are

$$\begin{aligned} C_1 &= \Delta t - \tau\left(1-e^{-\Delta t/\tau}\right),\\ C_2 &= 2\tau^2\left(1-e^{-\Delta t/\tau}\right) - \tau\Delta t - \tau\Delta t e^{-\Delta t/\tau},\\ C_3 &= \frac{\Delta t^2}{2} - \tau\Delta t + \tau^2\left(1-e^{-\Delta t/\tau}\right). \end{aligned} \tag{3.11}$$

The analytical free-streaming flux $(F_{\boldsymbol{W}})_s^{f,w}$ contributed from the collisional particles is given as

$$(F_{\boldsymbol{W}})_s^{f,w} = \frac{1}{\Delta t}\int \boldsymbol{u}\cdot\boldsymbol{n}_s\left(C_4 g_0^h + C_5\boldsymbol{u}\cdot\boldsymbol{g}_{0x}^h\right)\boldsymbol{\Psi}\mathrm{d}\boldsymbol{u}, \tag{3.12}$$

where g_0^h denotes the equilibrium distribution function of the wave component. The macroscopic wave contribution is defined as $\boldsymbol{W}^h = \boldsymbol{W} - \boldsymbol{W}^p$, where $\boldsymbol{W}^p$ represents the macroscopic conservative variables of the particle component and g_{0x}^h is the spatial slope

https://doi.org/10.1017/jfm.2026.12223 Published online by Cambridge University Press

of g_0^h. The time integration coefficients are

$$C_4 = \tau\left(1 - e^{-\Delta t/\tau}\right) - \Delta t e^{-\Delta t/\tau},$$
$$C_5 = \tau\,\Delta t e^{-\Delta t/\tau} - \tau^2\left(1 - e^{-\Delta t/\tau}\right) + \frac{\Delta t^2}{2} e^{-\Delta t/\tau}. \tag{3.13}$$

The net particle flux $(F_{\boldsymbol{W}})_s^{f,p}$ is calculated as

$$(F_{\boldsymbol{W}})_s^{f,p} = \sum_{k \in P_{\partial\Omega_i^+}} \boldsymbol{W}_{P_k} - \sum_{k \in P_{\partial\Omega_i^-}} \boldsymbol{W}_{P_k}, \tag{3.14}$$

where $\boldsymbol{W}_{P_k} = (m_k, m_k \boldsymbol{v}_k, (1/2) m_k \boldsymbol{v}_{\boldsymbol{k}}^2)$, $P_{\partial\Omega_i^-}$ is the index set of the particles streaming out of cell Ω_i during a time step and $P_{\partial\Omega_i^+}$ is the index set of the particles streaming into cell Ω_i. Finally, the update formula for conservative variables is

$$\boldsymbol{W}_i^* = \boldsymbol{W}_i^n - \sum_s \frac{\Delta t}{|\Omega_i|} |l_s| (F_{\boldsymbol{W}})_s^g - \sum_s \frac{\Delta t}{|\Omega_i|} |l_s| (F_{\boldsymbol{W}})_s^{f,w} + \frac{1}{|\Omega_i|} (F_{\boldsymbol{W}})_s^{f,p}. \tag{3.15}$$

For the multi-species energy exchange stage $\mathcal{L}_3^{fl}$, we first update the macroscopic temperatures of the heavy particles and electrons. We compute the energy exchange term S_{eh} using equation (2.22) and use it to adjust the electron temperature. We then evaluate $S_{he} = -S_{eh}$ and apply it to adjust the heavy-particle temperature. After updating the macroscopic temperature of the heavy particles, we scale the velocities of the microscopic particles to ensure consistency between the microscopic and macroscopic temperatures. In this manner, $\mathcal{L}_3$ is solved both macroscopically and microscopically.

3.3. *Iteration method for ionisation process*

The ionisation step for $\mathcal{L}_2^{fl}$ proceeds in two steps. First, we solve the transport equation for the degree of ionisation. Second, we solve the ordinary differential equation system that governs the energy change due to ionisation and the evolution of the ionisation degree.

Step 1: transport equation. The degree of ionisation α satisfies

$$\frac{\partial(\rho\alpha)}{\partial t} + \nabla \cdot (\rho\alpha \boldsymbol{U}) = 0. \tag{3.16}$$

To suppress numerical instability across the shock layer, we discretise this equation using the Lax–Friedrichs scheme.

Step 2: coupled ionisation system. The system reads

$$\begin{cases} \dfrac{\partial \rho\alpha}{\partial t} = m_h \dot{n}_e, \\ \dfrac{\partial(\rho E_h)}{\partial t} = -\epsilon_{ion}[\dot{n}_e]_{Ar}, \\ \dfrac{\partial(\rho E_e)}{\partial t} = -\epsilon_{ion}[\dot{n}_e]_e. \end{cases} \tag{3.17}$$

https://doi.org/10.1017/jfm.2026.12223 Published online by Cambridge University Press

Algorithm 1: Picard iteration for the coupled two-temperature ionisation system.

Input: Initial guess α_0, T_{h0}, T_{e0}; time step Δt; tolerance R_{tol}
Output: Converged degree of ionization α and temperature T_h and T_e
Set $\alpha^* \leftarrow \alpha_0$, $T_h^* \leftarrow T_{h0}$, $T_e^* \leftarrow T_{e0}$;
repeat
  Compute $\dfrac{\partial \alpha^*}{\partial t} = f(\alpha^*, T_h^*, T_e^*)$ and $\dfrac{\mathrm{d}T_h^*}{\mathrm{d}t} = g(\alpha^*, T_h^*)$ and $\dfrac{\mathrm{d}T_e^*}{\mathrm{d}t} = h(\alpha^*, T_e^*)$ using equation (3.2);
  Update:

$$\alpha_{new} \leftarrow \alpha_0 + \boldsymbol{\Delta t}\,\frac{\partial \alpha^*}{\partial t},$$
$$T_{h,new} \leftarrow T_{h0} + \boldsymbol{\Delta t}\,\frac{\mathrm{d}T_h^*}{\mathrm{d}t},$$
$$T_{e\ new} \leftarrow T_{e0} + \boldsymbol{\Delta t}\,\frac{\mathrm{d}T_e^*}{\mathrm{d}t}.$$

  if $|\alpha_{new} - \alpha^*| \geq R_{\alpha,tol}$ *or* $|T_{h,new} - T_h^*| \geq R_{Th,\,tol}$ *or* $|T_{e,new} - T_e^*| \geq R_{Te,\,tol}$ **then**
    $\alpha^* \leftarrow \alpha_{new}$, $T_h^* \leftarrow T_{h,new}$, $T_e^* \leftarrow T_{e,new}$;
    Continue with next iteration;
  end
until $|\alpha_{new} - \alpha^*| < R_{\alpha,tol}$ *and* $|T_{h,new} - T_h^*| < R_{Th,\,tol}$ *and* $|T_{e,new} - T_e^*| < R_{Te,\,tol}$;
return $\alpha_{new}, T_{h,new}, T_{e,new}$;

We rewrite it in the simpler form

$$\begin{aligned}
\frac{\mathrm{d}\alpha}{\mathrm{d}t} &= f(\alpha, T_h, T_e),\\
\frac{\partial T_h}{\partial t} &= g(\alpha, T_h),\\
\frac{\partial T_e}{\partial t} &= h(\alpha, T_e),
\end{aligned} \tag{3.18}$$

with

$$\begin{aligned}
f(\alpha, T_h, T_e) &= n(1-\alpha)\left[k_{fA}(1-\alpha) + k_{fe}\alpha\right] - n^2\alpha^2\left[k_{rA}(1-\alpha) + k_{re}\alpha\right],\\
g(\alpha, T_h) &= -\frac{2}{3}\Theta_{ion}\left[k_{fA}(1-\alpha)^2 n - k_{rA}(1-\alpha)\alpha^2 n^2\right],\\
h(\alpha, T_e) &= -\frac{2}{3}\Theta_{ion}\left[k_{fe}(1-\alpha)n - k_{re}(\alpha n)^2\right].
\end{aligned} \tag{3.19}$$

We solve the coupled system using Picard iteration, as outlined in Algorithm 1.

https://doi.org/10.1017/jfm.2026.12223 Published online by Cambridge University Press

M_1	u_1 (m s^{-1})	Frozen state			Equilibrium state			
		T_{fr} (K)	U_{fr} (m s^{-1})	ρ_{fr} (kg m^{-3})	T_{eq} (K)	U_{eq} (m s^{-1})	ρ_{eq} (kg m^{-3})	α_{eq}
9.7	3130	9082.8	807.4	8.2743×10^{-2}	8797.5	774.3	8.6281×10^{-2}	4.0915×10^{-3}
10.0	3226	9636.9	830.8	8.2894×10^{-2}	9182.6	780.5	8.8238×10^{-2}	6.4567×10^{-3}
10.3	3323	10207.9	854.3	8.3033×10^{-2}	9535.8	783.2	9.0567×10^{-2}	9.4700×10^{-3}
10.5	3388	10597.9	870.0	8.3119×10^{-2}	9754.4	783.5	9.2296×10^{-2}	1.1819×10^{-2}
10.7	3452	10995.4	885.7	8.3201×10^{-2}	9960.8	782.7	9.4144×10^{-2}	1.4419×10^{-2}
11.0	3549	11605.8	909.3	8.3315×10^{-2}	10249.6	780.2	9.7101×10^{-2}	1.8753×10^{-2}
11.5	3710	12660.5	948.6	8.3487×10^{-2}	10684.9	773.5	1.0240×10^{-1}	2.6994×10^{-2}

Table 1. Calculated post-shock frozen and equilibrium properties of non-equilibrium argon flows at various incident Mach numbers. Free-stream conditions: $T_1 = 300.0$ K, $p_1 = 1333.22$ Pa (10.0 mmHg) and $\rho_1 = 2.1345 \times 10^{-2}$ kg m^{-3}.

3.4. *Auxiliary differential equation*

To avoid possible instability of the plasma oscillation period, we implicitly couple the current density equation and Ampere's law to solve. The system is

$$\begin{cases} \dfrac{\partial \boldsymbol{J}}{\partial t} + \nu_{eh}\boldsymbol{J} = \epsilon_0 \omega_p^2 \boldsymbol{E}, \\ \dfrac{\partial \boldsymbol{E}}{\partial t} = -\dfrac{1}{\epsilon_0}\boldsymbol{J}. \end{cases} \tag{3.20}$$

These two equations constitute a coupled system that reveals the interaction of plasma and electric field. Discretise the time derivative term with the Crank–Nicolson scheme and we can get an explicit expression of this system as

$$\begin{cases} \boldsymbol{E}^{n+1} = \dfrac{1}{C}\left[\left(1 + \dfrac{\nu_{eh}\Delta t}{2} - \dfrac{\omega_p^2 \Delta t^2}{4}\right)\boldsymbol{E}^n - \dfrac{\Delta t}{\epsilon_0}\boldsymbol{J}^n\right], \\ \boldsymbol{J}^{n+1} = -\boldsymbol{J}^n - \dfrac{2\epsilon_0}{\Delta t}(\boldsymbol{E}^{n+1} - \boldsymbol{E}^n). \end{cases} \tag{3.21}$$

Here, $C = 1 + (\nu_{eh}\Delta t/2) + (\omega_p^2 \Delta t^2/4)$.

4. Validation

To assess the fidelity of the current ionisation module, we validate the simulation results against classic shock-tube measurements of Petschek & Byron (1957). Their experiment examines the ionising flow behind a strong normal shock propagating into quiescent argon. We reproduce this configuration by imposing a subsonic inflow at the left and right boundaries of the computational domain; the inflow gas enters un-ionised. The inflow state, which we refer to as the frozen state, follows from the standard Rankine–Hugoniot jump relations for a non-ionising shock (Hoffert & Lien 1967). At the right boundary, the flow attains its equilibrium state, characterised by a constant ionisation degree and steady values of all other variables. We compute this equilibrium state iteratively (Hoffert & Lien 1967). Table 1 lists several states computed for this validation study.

Figure 2 presents the spatial evolution of heavy-particle temperature (T_h), electron temperature (T_e) and the degree of ionisation (α) behind a Mach 10 normal shock. Downstream of the shock front, the initial frozen heavy-particle temperature is set to 9636.9 K, and the electron temperature is prescribed at 5000 K (as discussed by Hoffert

https://doi.org/10.1017/jfm.2026.12223 Published online by Cambridge University Press

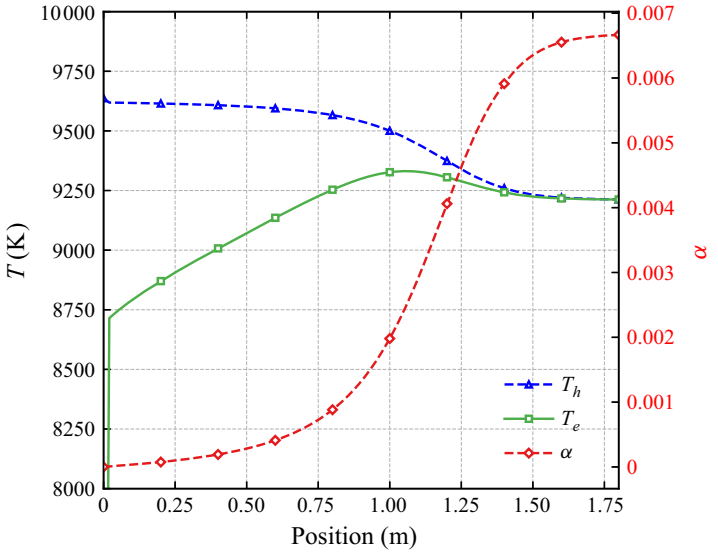


Figure 2. Variation of flow temperature and ionisation degree behind a normal shock.

and Lien (1967), the electron temperature relaxation profiles converge rapidly to a consistent value regardless of the specific initial frozen electron temperature assigned); the complete set of parameters appears in the accompanying table 1.

In the initial stage of the relaxation zone, T_h declines gradually. During this phase, atom–atom collisions drive TI, which acts as the primary ionisation mechanism. The overall ionisation rate, however, remains low because the forward rate constant for thermal impact ionisation is inherently small. Meanwhile, T_e rises steadily as energy transfers from the heavy particles to the electrons. In the subsequent stage, once the electron number density n_e surpasses a critical threshold, EI becomes the dominant process and triggers an exponential growth in the ionisation degree. During this second stage, T_h decreases much more steeply. This rapid decline reflects the role of EI as a substantial energy sink: it rapidly drains energy from the electron population, which is then replenished through efficient collisions with the heavy particles, thereby extracting energy from the heavy-particle reservoir. In the final stage, the system relaxes toward thermal and chemical equilibrium. Here, T_h and T_e equilibrate to a common value, and the ionisation degree approaches its asymptotic equilibrium limit.

Figure 3 demonstrates that the predicted ionisation relaxation time behind the normal shock successfully captures the experimental trends. All parameters are listed in table 1. The characteristic ionisation time is defined as $\tau = l/U_1$, where l is the relaxation length and U_1 is the free-stream velocity ahead of the shock. Because full thermochemical equilibrium is approached only asymptotically, a finite characteristic relaxation length must be introduced. Following Petschek and Byron (1957), we define this length as

$$l = x|_{\alpha=2^{-1/2}\alpha_{eq}}\,, \tag{4.1}$$

where x denotes the downstream distance from the shock front and α_{eq} is the equilibrium ionisation degree in the post-shock state. Overall, the comparison with experiments shows good agreement, confirming the accuracy of the present ionisation model.

https://doi.org/10.1017/jfm.2026.12223 Published online by Cambridge University Press

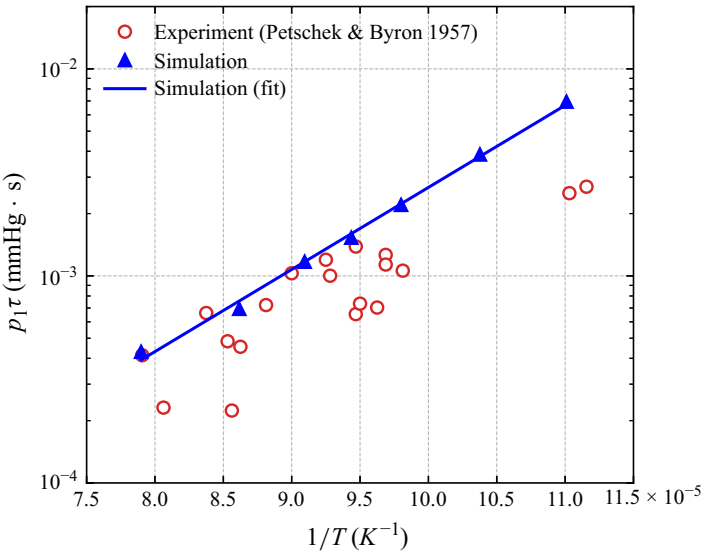


Figure 3. Variation of ionisation relaxation time behind normal shock waves in argon gas. The numerical predictions of the present model are compared against the experimental shock-tube data from Petschek and Byron (1957).

5. Non-equilibrium plasma formation around a cylinder

This section investigates hypersonic flow over a cylinder in the transitional regime at $Kn_\infty = 0.05$, where non-equilibrium effects are significant. We present the flow field results computed by the GKS and UGKWP methods, followed by an analysis of electromagnetic-wave scattering in § 6.

The Knudsen number characterises the degree of rarefaction. The free-stream Knudsen number used in this study is defined as

$$Kn_\infty = \frac{\lambda_\infty}{L_{ref}}, \tag{5.1}$$

where λ_∞ is the molecular mean free path of the free-stream flow and L_{ref} is the characteristic length of the problem, taken as the cylinder diameter (2 m). In addition to the global Knudsen number, the local non-equilibrium is quantified by the gradient-length local Knudsen number

$$Kn_{Gll} = \frac{\lambda}{\rho/|\nabla\rho|}, \tag{5.2}$$

where λ is the local molecular mean free path.

We first compute the flow field using the continuum GKS and the multiscale UGKWP solver. The only difference between the two solvers is the flux evaluation: UGKWP employs the wave–particle formulation to capture arbitrary non-equilibrium distributions, whereas GKS employs the standard direct solver based on the Chapman–Enskog expansion. In the GKS, the collision time is bounded by $\tau = \min(\tau, \tau_{max})$, where τ_{max} is the upper bound of allowed tau for GKS to avoid excessive viscosity that would otherwise severely limit the time step. All other settings are kept the same. From the computed flow field, we obtain the electron number density and temperature, which are then put into the electromagnetic module to evaluate the scattering behaviours of the plasma generated inside the shock.

https://doi.org/10.1017/jfm.2026.12223 Published online by Cambridge University Press

Parameter	Value
Mach number	22
Knudsen number	0.05
Argon atomic mass	6.63×10^{-26} kg
Argon diameter variable hard sphere (VHS)	4.17×10^{-10} m
Incoming argon density	1×10^{-6} kg m^{-3}
Incoming argon velocity	6000 m s^{-1}
Incoming argon temperature	200 K
Wall temperature (isothermal)	200 K
Cylinder radius	1 m

Table 2. Simulation parameters for the rarefied argon flow around a cylinder.

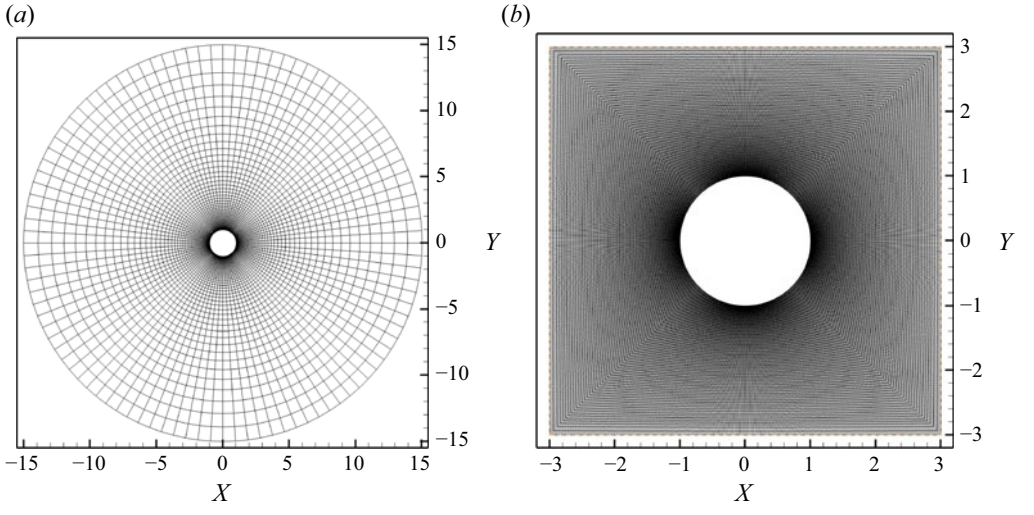


Figure 4. Computational domain and mesh for (*a*) the flow field and (*b*) the electromagnetic field.

For the fluid field simulation, the cylinder radius is $r = 1$ m. The computational mesh is generated by extrusion, with a first-layer height of approximately $0.02r$ and a total of 5000 cells, as shown in figure 4(*a*). For the electromagnetic field simulation, the same cylinder geometry is used, but with a different mesh, as illustrated in figure 4(*b*). The fluid solution is interpolated onto the electromagnetic mesh, which is then refined to 5 120 000 cells, corresponding to more than 100 points per wavelength, to ensure numerical accuracy. Table 2 lists the flow parameters. The Knudsen number is normalised by the diameter of the cylinder $L = 2$ m.

Figure 5 compares the temperature and electron number density contours from GKS (upper half) and UGKWP (lower half). In this transitional regime, significant non-equilibrium effects are observed. As shown in figure 5(*a*), UGKWP predicts a broader temperature distribution than GKS, reflecting its enhanced non-equilibrium transport capability relative to the purely diffusion-based GKS. Figure 5(*b*) shows the electron number density contours on a logarithmic scale. Two differences are notable: first, UGKWP predicts a broader extension of the ionised region into the upstream stagnation zone, consistent with the extended preheating layer captured by the temperature field;

https://doi.org/10.1017/jfm.2026.12223 Published online by Cambridge University Press

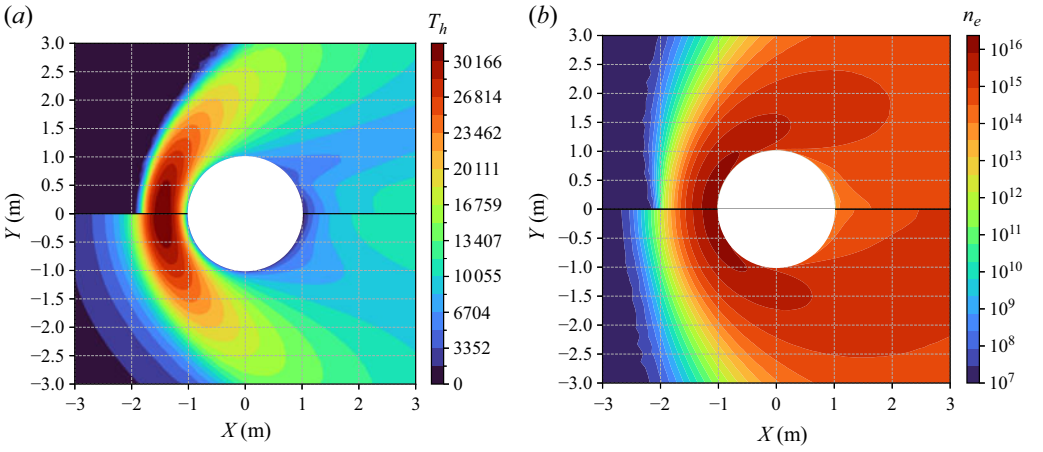


Figure 5. (*a*) Heavy-particle temperature and (*b*) electron number density contours at $Kn = 0.05$. The upper and lower halves correspond to the GKS and UGKWP solutions, respectively.

second, in the wake region, UGKWP yields higher temperature and then electron number densities than GKS, which is consistent with literature results (Lofthouse *et al.* 2008; Long *et al.* 2026). Figure 6 presents the local Knudsen number contours and its profile along the stagnation line. Three distinct peaks of Kn_{GII} are observed: one across the shock layer, where the flow field varies rapidly, one within the boundary layer and one in the wake region. The peak value exceeds 0.4, indicating that the flow locally exceeds the continuum regime. This suggests that a kinetic description is required in these regions.

Figure 7 compares the heavy-particle temperature and number density along the stagnation line predicted by GKS and UGKWP. The UGKWP results exhibit a pronounced increase in heavy-particle number density immediately adjacent to the wall, which enhances near-wall ionisation and consequently leads to a higher electron number density than that predicted by GKS, as shown in figure 8. This density enhancement may arise from non-local kinetic transport, whereby a fraction of heavy particles traverse the shock layer and penetrate into the near-wall region while retaining their wall-directed momentum, before collisions fully randomise their motion – an effect that may be underestimated by the near-equilibrium GKS description.

Elsewhere within the boundary layer, however, UGKWP predicts consistently lower temperatures than GKS, and GKS yields higher electron densities. This behaviour also arises from the distinct capability of each scheme to capture non-equilibrium transport. In GKS, the cold-wall effect remains confined to a very thin layer adjacent to the wall. The UGKWP, by contrast, captures non-local non-equilibrium transport, allowing the cold-wall influence to extend farther into the flow field. Meanwhile, the particle density reaches its maximum within the boundary layer due to strong compression, making this region the most favourable for ionisation. Given that the higher temperature predicted by GKS, combined with the high local density, promotes significantly more ionisation, GKS predicts higher electron number densities.

Figure 9 presents the electron number density along circular arcs at radii (*a*) $r = 1.01$ and (*b*) $r = 1.03$ m around the cylinder. In both cases, the UGKWP predictions exceed the GKS results, with the discrepancy increasing as the surface approaches the wall. This near-wall enhancement is associated with the higher heavy-particle number density predicted

https://doi.org/10.1017/jfm.2026.12223 Published online by Cambridge University Press

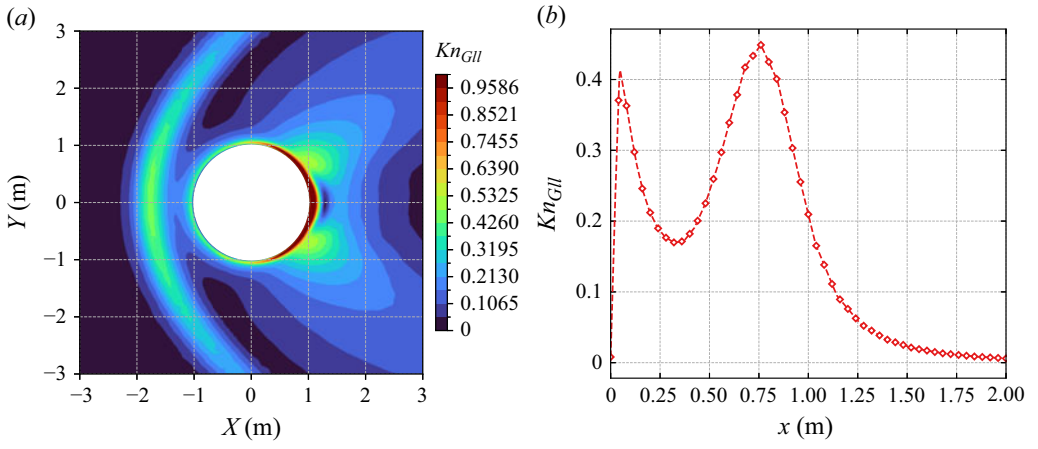


Figure 6. Local Knudsen number (*a*) contour and (*b*) profile along the stagnation line.

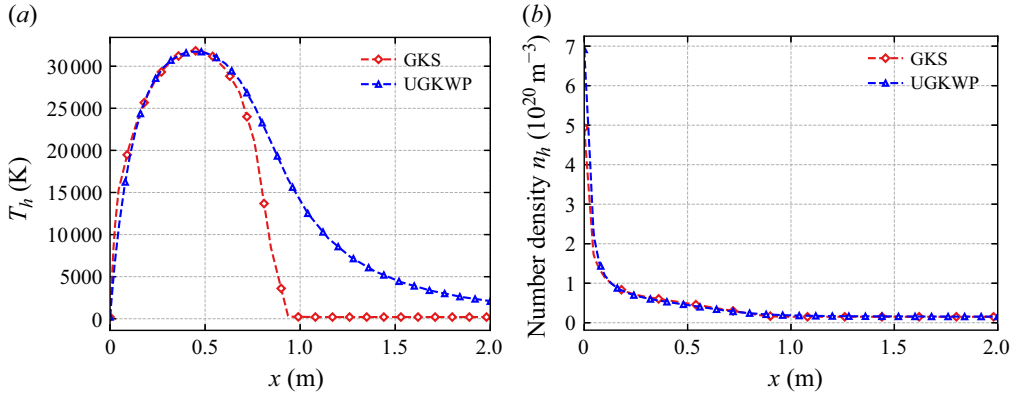


Figure 7. (*a*) Heavy-particle temperature and (*b*) number density along the stagnation line at $Kn = 0.05$.

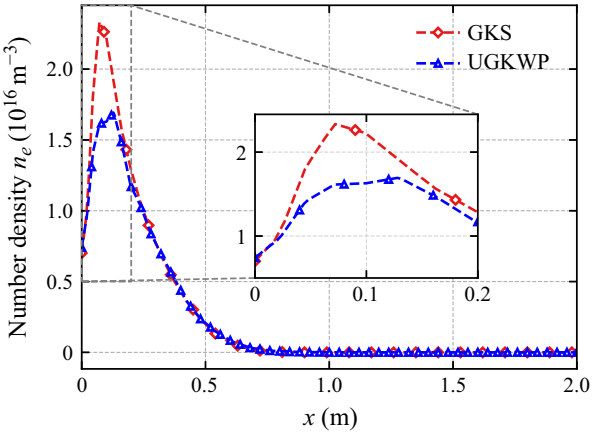


Figure 8. Electron number density along the stagnation line at $Kn = 0.05$.

https://doi.org/10.1017/jfm.2026.12223 Published online by Cambridge University Press

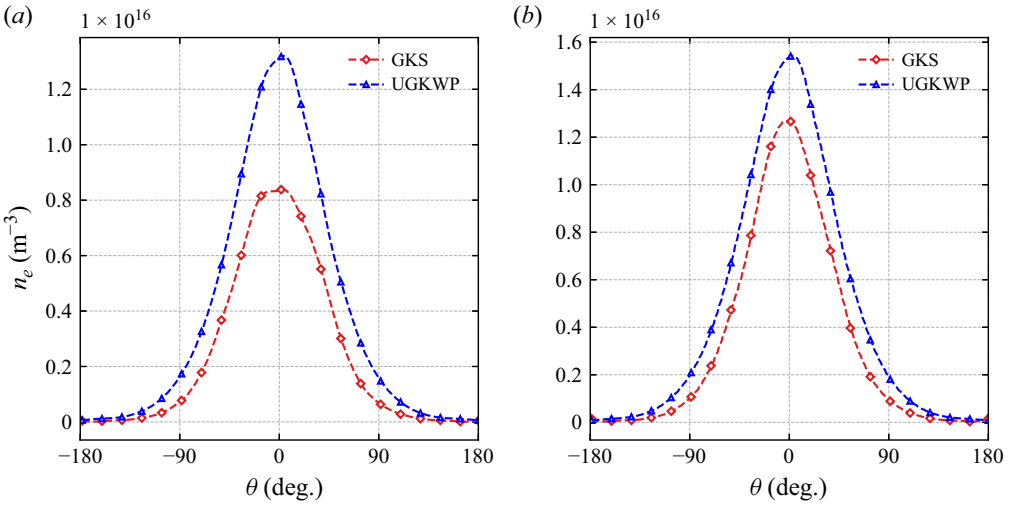


Figure 9. Electron number density along circular arcs at radii (*a*) $r = 1.01$ m and (*b*) $r = 1.03$ m.

by UGKWP, which promotes ionisation and leads to stronger local shielding than that predicted by GKS.

6. Electromagnetic-wave scattering by the plasma layer

Based on the computed flow fields, we next simulate electromagnetic-wave propagation to compare the scattering characteristics. The electromagnetic calculations are intended to provide a qualitative illustration of how rarefaction-induced changes in the plasma distribution affect wave propagation, rather than a quantitative evaluation of the global reflection and transmission coefficients.

The simulations are configured as follows. A transverse magnetic plane wave enters the domain at frequency f with components $E_z = \sin(2\pi f t)$ and $B_y = E_z/c$, where c denotes the speed of light. Two incident frequencies, 1.2 and 0.9 GHz, and two propagation directions –in the positive x-direction (from $(-1, 0)$ to $(1, 0)$) and at a 45 ° angle relative to the negative x-axis (from $(1, 1)$ to $(-1, -1)$) – are considered. The mesh setting is shown in the previous § 5 in figure 4(*b*). Absorbing boundary conditions are applied at the remaining boundaries to minimise spurious reflections. The cylinder surface is modelled as a perfect electrical conductor. All electromagnetic simulations are run up to a time of 2×10^{-8}s, corresponding to 24 and 18 complete wave periods for 1.2 and 0.9 GHz, respectively. Therefore, the instantaneous fields are compared at the same phase of the incident wave.

We first examine a high-frequency case at $f = 1.2$ GHz, in which the wave enters from the left boundary and propagates along the (−1,0) to (1,0) direction. The corresponding critical electron number density is approximately 1.8×10^{16} m^{-3}. At this frequency, the wave propagates freely through most of the shock layer, where the local electron number density remains below the critical value. Significant reflection occurs only in the immediate vicinity of the cylinder surface, where the electron number density exceeds the cutoff threshold.

Figure 10 presents the corresponding contours of permittivity and conductivity, defined as

https://doi.org/10.1017/jfm.2026.12223 Published online by Cambridge University Press

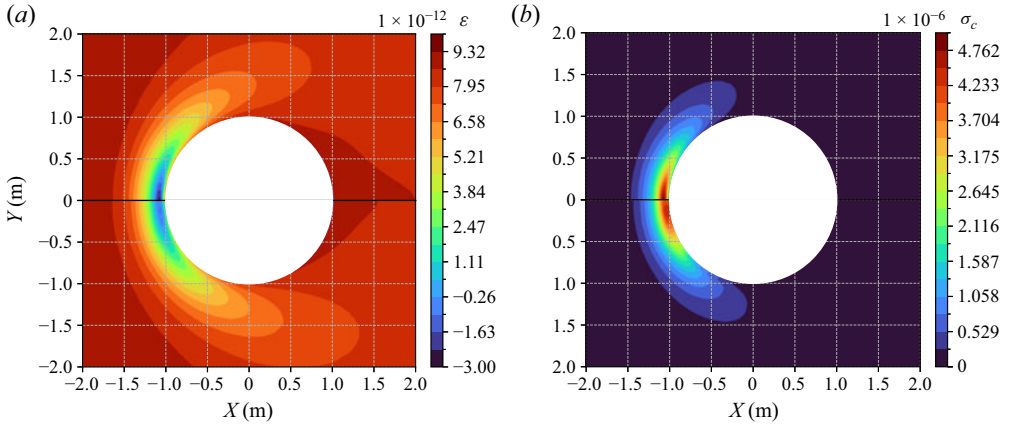


Figure 10. (*a*) Permittivity ε and (*b*) conductivity σ_c at $f = 1.2$ GHz. The upper and lower halves correspond to the GKS and UGKWP flow fields, respectively.

$$\varepsilon = \varepsilon_0 \left(1 - \frac{\omega_p^2}{\omega^2 + \nu_{eh}^2}\right), \qquad \sigma_c = \frac{\varepsilon_0 \omega_p^2 \nu_{eh}}{\omega^2 + \nu_{eh}^2}, \tag{6.1}$$

where $\omega = 2\pi f$ is the angular frequency. The upper half of each contour uses the GKS flow field, and the lower half uses the UGKWP results. As shown in figure 10(*a*), negative permittivity is confined to the region immediately adjacent to the cylinder surface; elsewhere, the permittivity remains positive, allowing wave transmission. The upper half exhibits more negative permittivity than the lower half, reflecting the higher peak electron number density in the GKS solution. Similarly, GKS-based plasma field produces larger conductivity around the main electron-density peak in the stagnation shock layer, whereas UGKWP-based plasma field yields locally enhanced conductivity in the region immediately adjacent to the wall.

Figure 11 compares the magnitudes of the electric and magnetic fields. The upper half of each contour corresponds to the GKS-based plasma profile, and the lower half to the UGKWP-based profile. The wave propagates through most of the shock layer and decays only in the immediate vicinity of the cylinder surface, where the electron number density exceeds the critical value. The amplitude enhancement observed within the plasma layer may be attributed to resonance effects associated with evanescent wave behaviour (White & Chen 1974).

Figure 12(*a*) shows the E_z profile along the stagnation line. At the selected phase, the GKS-based plasma profile exhibits a more pronounced reflected-wave pattern along the stagnation line, consistent with its higher peak electron number density. Figure 12(*b*) presents the field distribution along a circular arc at $r = 1.01$ m. Near the cylinder surface, UGKWP predicts a lower instantaneous field amplitude than GKS. This behaviour is consistent with the higher near-wall electron density, as shown in figure 8, indicating stronger local shielding and reduced field penetration. Consequently, UGKWP predicts stronger near-wall shielding, whereas GKS exhibits a stronger reflection tendency in the stagnation shock layer.

We next examine a lower-frequency case at $f = 0.9$ GHz. The corresponding critical electron number density is approximately 1.0×10^{16} m^{-3}. Figure 13 shows the permittivity and conductivity contours at this frequency. Compared with the 1.2 GHz case (figure 10*a*), the negative-permittivity region expands significantly, consistent with the

https://doi.org/10.1017/jfm.2026.12223 Published online by Cambridge University Press

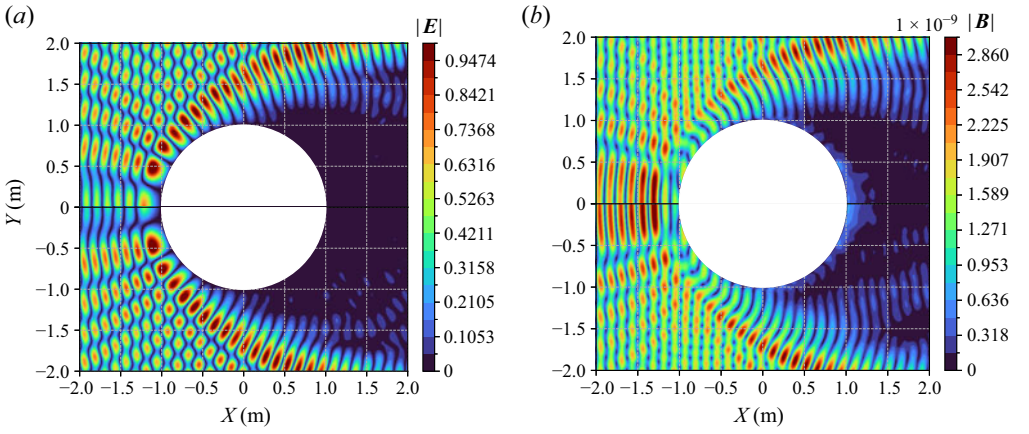


Figure 11. The (*a*) $|\boldsymbol{E}|$ and (*b*) $|\boldsymbol{B}|$ contours at $f = 1.2$ GHz. The upper and lower halves correspond to the GKS and UGKWP flow fields, respectively.

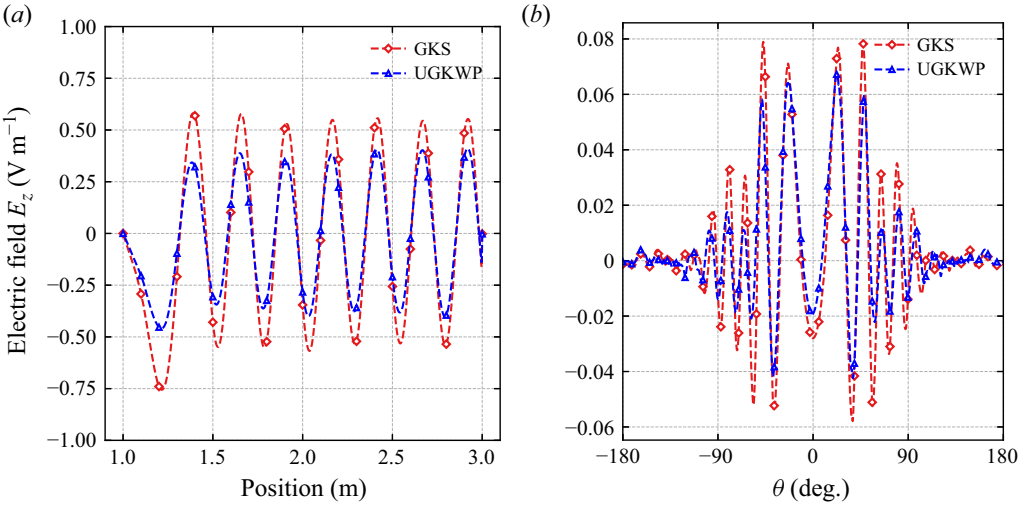


Figure 12. The E_z profiles (*a*) along the stagnation line and (*b*) along a circular arc at $r = 1.01$ m, at $f = 1.2$ GHz.

lower cutoff frequency. The conductivity contours (figure 13*b*) exhibit a similar trend, showing larger values in the same near-wall region.

Figure 14 shows the electromagnetic field magnitude contours at $f = 0.9$ GHz. At this frequency, the blackout region expands significantly, as evident in figure 14(*a*). The stagnation-line profile, shown in figure 15(*a*), exhibits a similar trend to the 1.2 GHz case: GKS reflects more signal than UGKWP, consistent with its higher peak electron number density. Figure 15(*b*) presents the E_z field along a circular arc at $r = 1.03$ m. Near the stagnation region (0 degrees), UGKWP predicts a weaker signal than GKS, but the trend reverses in the wake, where the UGKWP signal gradually exceeds that of GKS.

In both frequency cases, a consistent trend emerges: GKS predicts stronger reflection tendency in the stagnation region due to its higher peak electron number density, while UGKWP predicts more severe signal attenuation tendency near the cylinder surface.

https://doi.org/10.1017/jfm.2026.12223 Published online by Cambridge University Press

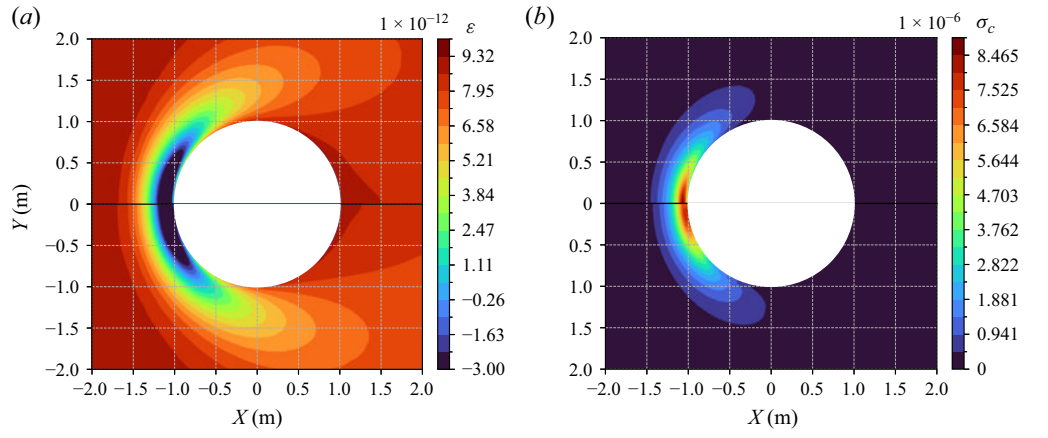


Figure 13. (*a*) Permittivity ε and (*b*) conductivity σ_c at $f = 0.9$ GHz. The upper and lower halves correspond to the GKS and UGKWP flow fields, respectively.

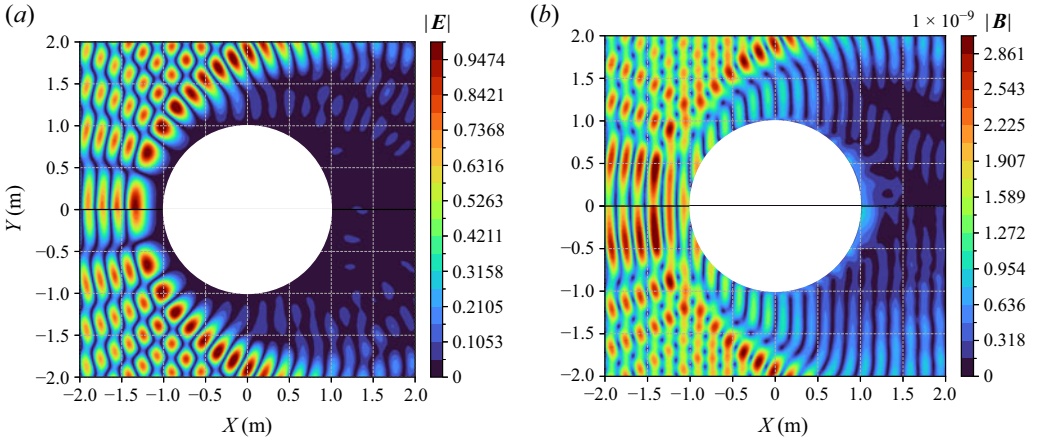


Figure 14. The (*a*) $|\boldsymbol{E}|$ and (*b*) $|\boldsymbol{B}|$ contours at $f = 0.9$ GHz. The upper and lower halves correspond to the GKS and UGKWP flow fields, respectively.

These contrasting behaviours arise from the inability of the continuum GKS model to capture the non-equilibrium transport processes that govern the boundary-layer structure and thus ionisation distribution.

We next consider a case where the incident wave propagates from the $(1, 1)$ to the $(-1, -1)$ direction at 0.9 GHz, as shown in figure 16. In contrast to the previous case with wave propagation along the $(-1, 0)$ to $(1, 0)$ direction (figure 14), the signal now reaches the cylinder surface. This is because the electron number density in the wake region is lower than in the stagnation region, as seen in figure 5(*b*). Despite both methods predicting wave transmission, the GKS and UGKWP results differ much more significantly in this oblique-incidence case than in the previous one. The magnitude and phase of the electromagnetic fields show distinctly different distributions. This discrepancy arises from the larger deviations in electron number density predicted by the two methods in the wake region, where the flow becomes more rarefied (figure 6*a*). In this region,

https://doi.org/10.1017/jfm.2026.12223 Published online by Cambridge University Press

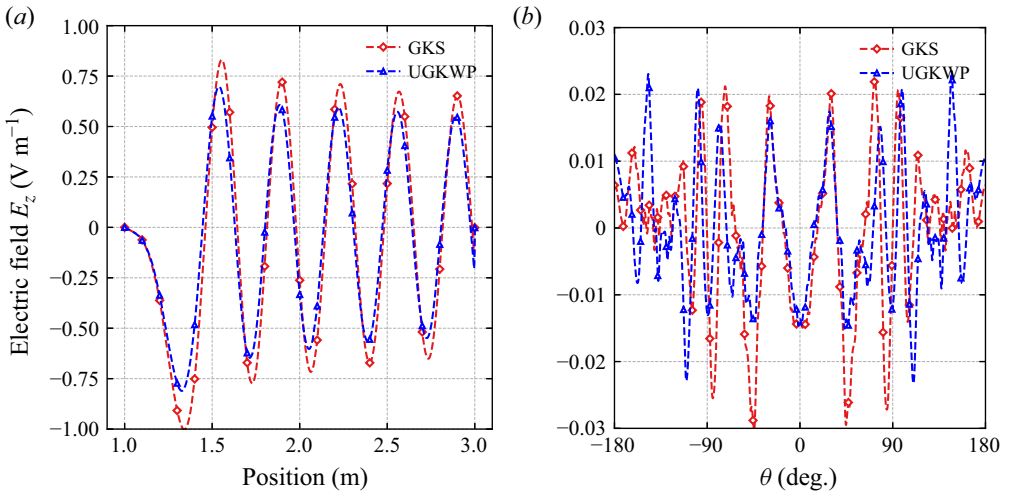


Figure 15. The E_z profiles (*a*) along the stagnation line and (*b*) along a circular arc at $r = 1.03$ m, at $f = 0.9$ GHz.

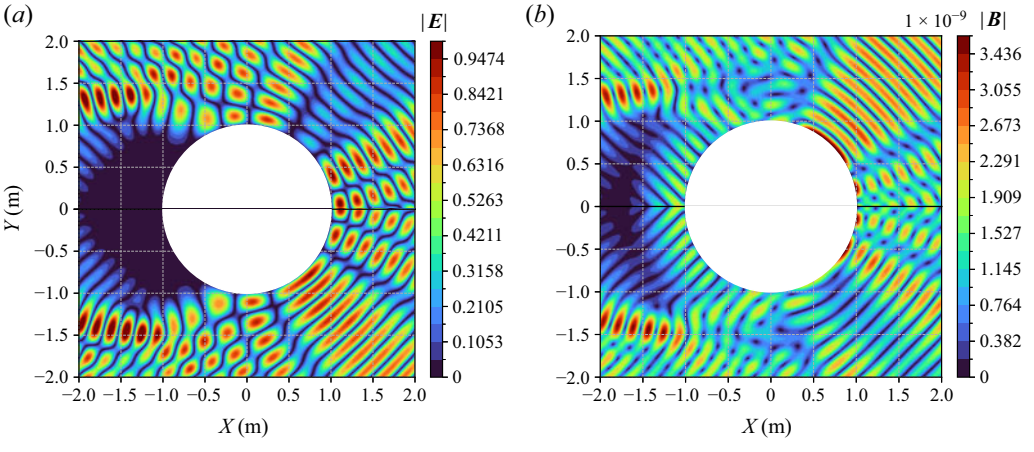


Figure 16. The (*a*) $|\boldsymbol{E}|$ and (*b*) $|\boldsymbol{B}|$ contours at $f = 0.9$ GHz. The incident wave direction comes from (1,1) to $(-1,-1)$. The upper and lower halves correspond to the GKS and UGKWP flow fields, respectively.

the continuum assumption fails, leading to substantial differences between the two predictions. These results highlight the importance of using a multiscale method to accurately predict the flow field in the wake region.

7. Conclusions

This paper has developed and validated a hybrid kinetic-fluid framework for simulating partially ionised argon plasmas in high-speed transitional flows. The main contributions and findings are summarised as follows.

First, a coupled kinetic-fluid model is established for heavy particles and electrons. The heavy-particle component is described by a kinetic equation with BGK-type elastic

https://doi.org/10.1017/jfm.2026.12223 Published online by Cambridge University Press

collision operator, solved by the UGKWP method, which seamlessly bridges the rarefied and continuum regimes. The electron temperature is advanced by a macroscopic energy equation that incorporates elastic collisions and ionisation energy loss. The coupling between the two is maintained through the ionisation-degree equation and the electron–heavy energy exchange term. The ionisation model, including both thermal and EI, is integrated and validated against shock-tube measurements. The predicted ionisation relaxation times show good agreement with experimental data, confirming the fidelity of the chemistry module.

Second, application to a Mach 22 cylinder flow at $Kn = 0.05$ reveals distinct differences between UGKWP and GKS predictions. Firstly, UGKWP predicts an increase in heavy-particle number density immediately adjacent to the wall, which enhances ionisation and elevates the near-wall electron number density. Secondly, within the boundary layer, UGKWP predicts a cooler thermal profile due to non-equilibrium transport, which reduces ionisation relative to GKS. In contrast, the GKS solution confines the cold-wall effect to a very thin layer and retains higher temperatures in the boundary layer, leading to overestimated electron densities in the stagnation region than those predicted by UGKWP. Thirdly, in the wake, UGKWP predicts a higher electron number density than GKS due to the higher temperature predicted by UGKWP in that region.

Third, electromagnetic-wave simulations show that these differences in plasma distribution have a direct impact on scattering behaviour. At both 1.2 and 0.9 GHz, the GKS-based plasma field exhibits a more pronounced reflected-wave pattern in the stagnation region, consistent with its higher peak electron number density. In contrast, the UGKWP-based plasma field exhibits reduced field penetration near the cylinder surface, consistent with the enhanced near-wall electron density. In the rear and wake regions, the discrepancies between GKS and UGKWP become even more pronounced due to the higher degree of rarefaction there, underscoring the necessity of employing a multiscale solver for accurate predictions in these areas. These contrasting patterns reflect the inability of continuum models to capture the non-equilibrium transport processes that govern boundary-layer structure and ionisation distribution.

In summary, the present work demonstrates that multiscale methods such as UGKWP are important for resolving non-equilibrium plasma formation and electromagnetic blackout in transitional hypersonic flows. These results establish a link between multiscale non-equilibrium transport, plasma formation and electromagnetic blackout in such flow regimes. Future work will extend the framework to air mixtures and incorporate radiation transport, as well as explore three-dimensional configurations with realistic vehicle geometries.

Acknowledgements. The first author would like to thank W. Long for the valuable discussions on the project.

Funding. This current work was supported by National Key R&D Program of China (Grant Nos. 2022YFA1004500), National Natural Science Foundation of China (92371107) and the Hong Kong Research Grant Council (16208324).

Declaration of interests. The authors report no conflict of interest.

Appendix A. Derivation of the heavy-particle Boltzmann equation

We begin with the complete set of Boltzmann equations for neutral atoms (n), singly charged ions (i) and electrons (e) in a partially ionised argon plasma

https://doi.org/10.1017/jfm.2026.12223 Published online by Cambridge University Press

$$\begin{aligned}
\frac{\partial f_n}{\partial t} + \boldsymbol{u}\cdot\nabla_{\boldsymbol{x}} f_n &= Q_n^{el} + Q_n^{ion},\\
\frac{\partial f_i}{\partial t} + \boldsymbol{u}\cdot\nabla_{\boldsymbol{x}} f_i + \frac{e\boldsymbol{E}}{m_i}\cdot\nabla_{\boldsymbol{u}} f_i &= Q_i^{el} + Q_i^{ion},\\
\frac{\partial f_e}{\partial t} + \boldsymbol{u}\cdot\nabla_{\boldsymbol{x}} f_e - \frac{e\boldsymbol{E}}{m_e}\cdot\nabla_{\boldsymbol{u}} f_e &= Q_e^{el} + Q_e^{ion}.
\end{aligned} \tag{A1}$$

Here, $f_s(\boldsymbol{x}, \boldsymbol{u}, t)$ is the velocity distribution function of species s, e is the elementary charge, $\boldsymbol{E}$ is the electric field and Q_s^{el}, Q_s^{ion} denote the elastic and ionisation–recombination collision operators, respectively. The ion and electron masses are m_i and m_e; the neutral and ion masses are taken as equal ($m_h \equiv m_n \approx m_i$).

In this study, we suppose neutral atoms and ions are tightly coupled by frequent elastic collisions and charge-exchange reactions. Consequently they relax to a common velocity distribution on a time scale much shorter than that of the macroscopic flow scale. We can therefore assume that f_n and f_i share the same functional form and differ only by their relative number densities. Introducing the heavy-particle distribution function

$$f_h(\boldsymbol{x}, \boldsymbol{u}, t) \equiv f_n + f_i, \tag{A2}$$

and the ionisation fraction

$$\alpha \equiv \frac{n_i}{n_n + n_i}, \qquad n_s = \frac{1}{m_h}\int f_s \,\mathrm{d}\boldsymbol{u}, \tag{A3}$$

the individual distributions are expressed as

$$f_n = (1-\alpha) f_h, \qquad f_i = \alpha f_h. \tag{A4}$$

Adding the evolution equations for f_n and f_i, and making use of the relations above, yields

$$\frac{\partial f_h}{\partial t} + \boldsymbol{u}\cdot\nabla_{\boldsymbol{x}} f_h + \alpha\frac{e\boldsymbol{E}}{m_h}\cdot\nabla_{\boldsymbol{u}} f_h = Q_n^{el} + Q_i^{el} + Q_n^{ion} + Q_i^{ion}. \tag{A5}$$

Here, $Q_n^{el} + Q_i^{el}$ can be expressed as the sum of two contributions: $Q_{hh}^{el}(f_h) + Q_{he}^{el}(f_h, f_e)$, describing elastic collisions among heavy particles and between heavy particles and electrons, respectively.

References

Angus, J.R., Dun, J., Farmer, W., Geyko, V., Grote, D., Larson, D., van de, W., Johannes, J. & Zimmerman, G. 2025 Kinetic study of strong shock waves in fully ionized plasmas. *Phys. Rev. E* **112** (6), 065201.

Bird, G.A. 1994 *Molecular Gas Dynamics and the Direct Simulation of Gas Flows*. Oxford University Press.

Boyd, I.D. & Schwartzentruber, T.E. 2017 *Nonequilibrium Gas Dynamics and Molecular Simulation*, vol. 42. Cambridge University Press.

Braginskii, S.I. 1965 Transport processes in a plasma. *Rev. Plasma Phys.* **1**, 205.

Cao, J., Wei, Y., Long, W., Zhong, C. & Xu, K. 2026 Adaptive criterion and modification of wave-particle decomposition in ugkwp method for high-speed flow simulation. *Comput. Fluids* **305**, 106896.

Hoffert, M.I. & Lien, H. 1967 Quasi-one-dimensional, nonequilibrium gas dynamics of partially ionized two-temperature argon. *Phys. Fluids* **10** (8), 1769–1777.

Ivanov, M.S. & Gimelshein, S.F. 1998 Computational hypersonic rarefied flows. *Annu. Rev. Fluid Mech.* **30** (1), 469–505.

Jaffrin, M.Y. 1965 Shock structure in a partially ionized gas. *Phys. Fluids* **8** (4), 606–625.

Kundrapu, M., Loverich, J., Beckwith, K., Stoltz, P., Shashurin, A. & Keidar, M. 2015 Modeling radio communication blackout and blackout mitigation in hypersonic vehicles. *J. Spacecr. Rockets* **52** (3), 853–862.

https://doi.org/10.1017/jfm.2026.12223 Published online by Cambridge University Press

LIU, C., LI, W., WANG, Y., SONG, P. & XU, K. 2023*a* An implicit unified gas-kinetic wave–particle method for radiative transport process. *Phys. Fluids* **35** (11), 112013.
LIU, C. & XU, K. 2021 Unified gas-kinetic wave-particle methods IV: multi-species gas mixture and plasma transport. *Adv. Aerodyn.* **3**, 1–31.
LIU, C., ZHU, Y. & XU, K. 2020 Unified gas-kinetic wave-particle methods I: continuum and rarefied gas flow. *J. Comput. Phys.* **401**, 108977.
LIU, H., YANG, X., ZHANG, C., JI, X. & XU, K. 2025 Unified gas-kinetic wave-particle method for multiscale phonon transport. *Phys. Rev. E* **112** (6), 065304.
LIU, Y.G., ZHANG, S., GAO, T.S., XU, Y., JIANG, T. & SONG, Z.X. 2023*b* Analysis of electromagnetic scattering from hypersonic vehicle coated with non-uniform plasma sheath based on FVTD method. *Phys. Plasmas* **30** (6), 063502.
LOFTHOUSE, A.J., SCALABRIN, L.C. & BOYD, I.D. 2008 Velocity slip and temperature jump in hypersonic aerothermodynamics. *J. Thermophys. Heat Transfer* **22** (1), 38–49.
LONG, W., CAO, J., ZHANG, Y. & XU, K. 2026 On the applicability of the gas-kinetic scheme with kinetic boundary conditions for near-continuum hypersonic flows. arXiv:2605.23303.
LONG, W., WEI, Y. & XU, K. 2024 Nonequilibrium flow simulations using unified gas-kinetic wave-particle method. *AIAA J.* **62** (4), 1411–1433.
MORGAN, E.J. & MORRISON, R.D. 1965 Ionization rates behind shock waves in argon. *Phys. Fluids* **8** (9), 1608–1615.
PETSCHEK, H. & BYRON, S. 1957 Approach to equilibrium Ionization behind strong shock waves in argon. *Ann. Phys* **1** (3), 270–315.
PU, Z., LIU, C. & XU, K. 2024*a* Gas-kinetic scheme for partially ionized plasma in hydrodynamic regime. *J. Comput. Phys.* **505**, 112905.
PU, Z., LONG, W. & XU, K. 2024*b* A gas-kinetic scheme for maxwell equations. arXiv:2412.16845.
PU, Z. & XU, K. 2025 Unified gas-kinetic wave-particle method for multiscale flow simulation of partially ionized plasma. *J. Comput. Phys.* **530**, 113918.
PU, Z. & XU, K. 2026 Electromagnetic flow control in hypersonic rarefied environment. *J. Fluid Mech.* **1033**, A37.
SUN, H., WANG, J., HAN, Y., CUI, Z., SUN, P., SHI, X. & ZHAO, W. 2018 Backward scattering characteristics of a reentry vehicle enveloped by a hypersonic flow field. *Intl J. Antennas Propag.* **2018** (1), 5478580.
SUTTON, G.W. & SHERMAN, A. 2006 *Engineering Magnetohydrodynamics*. Courier Dover Publications.
TAKAHASHI, Y. 2016 Advanced validation of cfd-fdtd combined method using highly applicable solver for reentry blackout prediction. *J. Phys. D: Appl. Phys.* **49** (1), 015201.
TAKAHASHI, Y., YAMADA, K. & ABE, T. 2014 Examination of radio frequency blackout for an inflatable vehicle during atmospheric reentry. *J. Spacecr. Rockets* **51** (2), 430–441.
TIAN, Y., HAN, Y.P., LING, Y.J. & AI, X. 2014 Propagation of terahertz electromagnetic wave in plasma with inhomogeneous collision frequency. *Phys. Plasmas* **21** (2), 023301.
WEI, Y., CAO, J. & XU, K. 2026 Unified gas-kinetic scheme for reactive flow with multi-scale transport and chemical non-equilibrium. *J. Comput. Phys.* **546**, 114514.
WHITE, R.B. & CHEN, F.F. 1974 Amplification and absorption of electromagnetic waves in overdense plasmas. *Plasma Phys.* **16** (7), 565–587.
YANG, X., SHYY, W. & XU, K. 2022 Unified gas-kinetic wave–particle method for gas–particle two-phase flow from dilute to dense solid particle limit. *Phys. Fluids* **34** (2).
YANG, X. & XU, K. 2026 Wave-particle based multiscale modeling and simulation of non-equilibrium turbulent flows. *Comput. Fluids* **317**, 107162.
YANG, X., ZHU, Y., LIU, C. & XU, K. 2025 Unified gas-kinetic wave-particle method for frequency-dependent radiation transport equation. *J. Comput. Phys.* **522**, 113587.
ZHU, Y., LIU, C., ZHONG, C. & XU, K. 2019 Unified gas-kinetic wave-particle methods II: multiscale simulation on unstructured mesh. *Phys. Fluids* **31** (6), 067105.

https://doi.org/10.1017/jfm.2026.12223 Published online by Cambridge University Press